Smart Structures and Systems, *Vol. 36, No. 2 (2025) 97-109*
https://doi.org/10.12989/sss.2025.36.2.097

Efficient detection of piezoelectric material defects in smart structures using nonlinear vibration and neural networks validation

Suleiman Ibrahim Mohammad *[1,2], Asokan Vasudevan [3,4], Abdelmajeed Alkasassbeh [5],
Omar Asad Ahmad [6], A'kif Alfugara [7], Nabil Ben Kahla [8,9], Nejib Ghazouani [10] and Murat Yaylacı [11,12]

[1] *Electronic Marketing and Social Media, Economic and Administrative Sciences, Zarqa University, Jordan*
[2] *Research follower, INTI International University, 71800 Negeri Sembilan, Malaysia*
[3] *Faculty of Business and Communications, INTI International University, 71800 Negeri Sembilan, Malaysia*
[4] *Shinawatra University, 99 Moo 10, Bangtoey, Samkhok, Pathum Thani 12160, Thailand*
[5] *Civil Engineering Department, Faculty of Engineering, Al al-Bayt University, Mafraq 25113, Jordan*
[6] *Department of Civil Engineering, Faculty of Engineering, Amman Arab University, 11953 Amman, Jordan*
[7] *Independent Researcher*
[8] *Department of Civil Engineering, College of Engineering, King Khalid University, PO Box 394, Abha 61411, Kingdom of Saudi Arabia*
[9] *Center for Engineering and Technology Innovations, King Khalid University, Abha 61421, Saudi Arabia*
[10] *Mining Research Center, Northern Border University, Arar 73213, Saudi Arabia*
[11] *Department of Civil Engineering, Recep Tayyip Erdogan University, 53100, Rize, Turkey*
[12] *Turgut Kıran Maritime Faculty, Recep Tayyip Erdogan University, 53900, Rize, Turkey*

(*Received June 7, 2025, Revised August 7, 2025, Accepted August 14, 2025*)

Abstract. This paper presents a new technique for detecting defects in piezoelectric materials located inside smart structures, mainly the troubleshooting of functionally graded piezoelectric (FGP) porous plates excited by an electric field. This research accounts for the Von-Karman nonlinearity to study the influence of mechanical and electrical loadings on the dynamic behavior of world material. Maxwell's equations are used to describe the coupling of electric fields with the piezoelectric properties of the plate, and porosity is closely examined for its impact on the defect detection process. Hamilton's principle is used to obtain the equations of motion, which can replicate the system's non-linear dynamics. The harmonic differential quadrature method (HDQM) is used to achieve numerical results, while equations governing the response of the system under different boundary conditions can be discretized appropriately. Deep learning models known as deep neural networks (DNN) are used to validate the mathematical model and extract more information from this complex, large dataset, which is obtained from these simulations. The DNN model provides a robust framework for detecting defects based on learning the complex relationships between different related features of the system, and its efficient classification aids in the detection and classification of defects. The study also explores the parameter selection and optimization in the DNN algorithm, so as to balance the model accuracy and computational efficiency. The results are important as they provide a cost-effective, accurate technique to detect defects in piezoelectric materials and help in smart structure health monitoring, which is a rapidly growing field. The experimental setup detailed in this research can form the basis for future developments of structural diagnostics and the implementation of smart materials in engineering applications.

Keywords: deep neural networks; dynamic simulation; functionally graded plates; nonlinear stress-strain equations; piezoelectric material defects

1. Introduction

Piezoelectric materials are characterized by their ability to generate electrical responses upon experiencing mechanical inputs and have attracted much interest over the last decades, mainly addressing applications in smart structures (Nanthakumar *et al*. 2016). In this way, when the structure is subjected to a mechanical stress (e.g., strain), vibration, or pressure load the materials generate electric charge which can be easily measured and, in an integrated fashion, provided as input to a downstream signal processing mechanism tuned for real-time monitoring/ response (Abbaspour *et al*. 2022). Due to their volatility, the piezoelectric materials has been used for a variety of applications that are beneficial in aerospace and the civil engineering, and in robotics this effect has been utilized to improve structural health, system efficiency as well as safety (Alrashdan 2020). Piezoelectric elements can function as sensors and actuators at the same time, making them ideal for smart structures which self-monitor, self-repair and adapt to changing conditions (Alshenawy *et al*. 2022). Functional gradients of piezoelectric materials, in which there is a gradual change in composition or properties, have been utilized to achieve improved mechanical and sensing performance as well as tailored functionality (Beni and Beni 2022), especially when dynamic loading results in stress distribution that cannot be

---

*Corresponding author, Ph.D.,
E-mail: dr_sliman@yahoo.com

http://www.techno-press.org/?journal=sss&subpage=7

ISSN: 1738-1584 (Print), 1738-1991 (Online)

considered uniform throughout the area. Furthermore, the advancement in piezoelectric structures has allowed to look forward to new ways of defect detection, energy harvesting and damage localization giving insight into complex system behavior (Al-Furjan *et al.* 2022). While these are all promising applications, a number of issues impede the real-world performance of piezoelectric materials including subjects to porosity, material deterioration in service, and nonlinearity under large deformations from their exhibited behavior (Arefi *et al.* 2018). Hence it is very important to study and optimize the behavior of piezo structures by varying conditions, as a key area of research to optimize modern engineering systems practicing these elements (Long *et al.* 2024).

Stability analysis, an elementary ingredient of structural engineering, revolves around identifying whether a system will remain at its steady state against external forces or perturbations (Al-Osta *et al.* 2021). In layman's term, it assesses the capability of various structures, materials or systems to withstand deformation, failure or collapses when subjected to different loading conditions (Foroutan *et al.* 2022). The main objective is the prediction of behavior of structures under static or dynamic loads such as safety and reliability (Zare *et al.* 2020). Stability in Structure Mechanics is subdivided into static and dynamic stability, each needing different analysis methods (Zerrouki *et al.* 2022). Dynamic stability refers to how the system behaves over time in relation to forces to which it may be subject. Stability is usually analyzed by using methods such as the Finite Element method, Lyapunov's direct method and energy based approaches (SafarPour *et al.* 2017), but in general to obtain these results it is necessary reoburecer dynamic equations of movement. In the case of nonlinear systems, analyses of stability are complicated due to significant deformations or the nonlinearity of materials (Barooti *et al.* 2017). Bifurcation theory is typically used to describe how the behavior of a system changes, such as when a stable region becomes unstable (Safarpour *et al.* 2021). For example, the design of structures including bridges, building and aerospace parts requires stability analysis since failure in these cases can lead to catastrophic consequences (Dastjerdi *et al.* 2020). With the development of smart and self-sustaining materials and structures, there has been an immense sophistication in systems simulation, whereby more and more advanced stability techniques are required today to guarantee that the engineered systems tend towards robustness (independent of their assembling variables) and resilience (to better respond to different failure patterns) (Rabczuk *et al.* 2019).

In practice, machine learning algorithms are becoming more and more crucial to map data to knowledge in a diverse set of such domains (Samaniego *et al.* 2020). It has significantly improved work in areas such as healthcare, finance and engineering by having power to process itself large complex datasets and detect patterns or trends (Wang *et al.* 2025). These algorithms automatically perform decision-making tasks, which often provides faster, more accurate and scalable solutions than traditional means (Guo *et al.* 2025). With advances in technology, machine learning algorithms have become more and more accurate, flexible and less expensive to train across a wide range of predictive analytics and optimization tasks (Anitescu *et al.* 2023). Machine learning is getting more important because it can help boost new ideas, cut down on mistakes people make, and help us make smarter choices based on facts (Liu *et al.* 2024).

This paper shows a cool way to find flaws in piezoelectric materials inside smart structures. It looks at FGP porous plates that have electricity running through them. The study uses Von-Karman nonlinearity to show how the plate moves and reacts, capturing the tricky relationship between mechanics and electricity inside the material. Maxwell's equations are used to show what the electric field does to the piezoelectric stuff, and how holes affect finding problems in the structure is looked at closely. Hamilton's principle is used to figure out the equations for how the FGP plate moves when things get nonlinear. For the math stuff, the HDQM is used to break down the system's equations, giving real answers to how the plate reacts in different situations. To check if this works and get better at finding flaws, DNN are used to show the link between how the system moves and what the flaw patterns look like. By teaching the DNN model with lots of info from simulations, this way gives really spot-on predictions but doesn't cost a ton to compute. The study shows how to tweak the DNN settings to make sure the model does well in tricky situations. The results add a lot to keeping an eye on structural health, giving a fresh, cheap way to find flaws in piezoelectric materials and setting the stage for what comes next in smart material check-ups.

2. The present problem model

A porous FGP plate has a length of a, a width of b, and a thickness of h, with electrodes attached to both the upper and lower surfaces, as shown in Fig. 1.

The FGP plate experiences an electric potential Φ when a voltage V_0 is applied across the electrodes. Refs. (Vel *et al.* 2004, Ramirez *et al.* 2006, Yang 2010, Bodaghi and Shakeri 2012) suggest that the structure consists of two piezoelectric materials.

2.1 Material properties

The properties of the piezoelectric porous plate display a smoothly varying gradient throughout its thickness, adhering to a power-law model and a uniform porous structure (Sharma 2022).

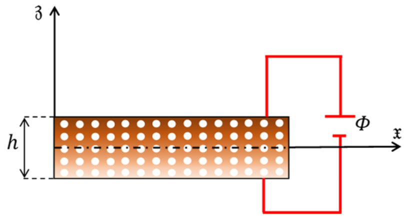

Fig. 1 A configuration of the presented FGP plate with porosity

$$
\begin{aligned}
\mathbb{C}_{ij}(\mathfrak{z}) &= \left(\mathbb{C}^u_{ij} - \mathbb{C}^b_{ij}\right)\left(\frac{2\mathfrak{z}+h}{2h}\right)^p + \mathbb{C}^b_{ij} - \frac{\beta}{2}\left(\mathbb{C}^u_{ij} + \mathbb{C}^b_{ij}\right),\\
\mathbb{e}_{ij}(\mathfrak{z}) &= \left(\mathbb{e}^u_{ij} - \mathbb{e}^b_{ij}\right)\left(\frac{2\mathfrak{z}+h}{2h}\right)^p + \mathbb{e}^b_{ij} - \frac{\beta}{2}\left(\mathbb{e}^u_{ij} + \mathbb{e}^b_{ij}\right),\\
\Xi_{ij}(\mathfrak{z}) &= \left(\Xi^u_{ij} - \Xi^b_{ij}\right)\left(\frac{2\mathfrak{z}+h}{2h}\right)^p + \Xi^b_{ij} - \frac{\beta}{2}\left(\Xi^u_{ij} + \Xi^b_{ij}\right),\\
\rho(\mathfrak{z}) &= \left(\rho^u - \rho^b\right)\left(\frac{2\mathfrak{z}+h}{2h}\right)^p + \rho^b - \frac{\beta}{2}\left(\rho^u_{ij} + \rho^b_{ij}\right).
\end{aligned}
\tag{1}
$$

Here, $\mathbb{C}_{ij}$, $\mathbb{e}_{ij}$, Ξ_{ij}, and ρ represent the elastic constants, piezoelectric constants, dielectric constants, and density, respectively. The superscripts u and b refer to the upper and bottom surfaces of the FGP plate, respectively. The symbol p denotes the volume fraction index, while β represents the porosity volume fraction.

3. Governing equations and boundary conditions

The three displacement components $\mathfrak{u}$, $\mathfrak{v}$ and $\mathfrak{w}$ can be modeled as (Guo *et al.* 2021)

$$
\begin{aligned}
\mathfrak{u}(\mathfrak{x},\mathfrak{y},\mathfrak{z},\mathrm{t}) &= \mathfrak{u}_0(\mathfrak{x},\mathfrak{y},\mathrm{t}) + \mathfrak{z}\mathfrak{u}_1(\mathfrak{x},\mathfrak{y},\mathrm{t}),\\
\mathfrak{v}(\mathfrak{x},\mathfrak{y},\mathfrak{z},\mathrm{t}) &= \mathfrak{v}_0(\mathfrak{x},\mathfrak{y},\mathrm{t}) + \mathfrak{z}\mathfrak{v}_1(\mathfrak{x},\mathfrak{y},\mathrm{t}),\\
\mathfrak{w}(\mathfrak{x},\mathfrak{y},\mathfrak{z},\mathrm{t}) &= \mathfrak{w}_0(\mathfrak{x},\mathfrak{y},\mathrm{t}).
\end{aligned}
\tag{2}
$$

where $\mathfrak{u}$, $\mathfrak{v}$, and $\mathfrak{w}$ are the displacements in the $\mathfrak{x}$-, $\mathfrak{y}$-, and $\mathfrak{z}$-directions, respectively. $\mathfrak{u}_0$, $\mathfrak{u}_1$, $\mathfrak{v}_0$, $\mathfrak{v}_1$, and $\mathfrak{w}_0$ are functions to be determined. The constitutive equations of Eq. (2) are given by

$$
\begin{aligned}
&\begin{Bmatrix}\varepsilon_{\mathfrak{x}}\\ \varepsilon_{\mathfrak{y}}\\ \gamma_{\mathfrak{x}\mathfrak{y}}\end{Bmatrix} = \begin{Bmatrix}\varepsilon^0_{\mathfrak{x}}\\ \varepsilon^0_{\mathfrak{y}}\\ \gamma^0_{\mathfrak{x}\mathfrak{y}}\end{Bmatrix} + \mathfrak{z}\begin{Bmatrix}\varepsilon^1_{\mathfrak{x}}\\ \varepsilon^1_{\mathfrak{y}}\\ \gamma^1_{\mathfrak{x}\mathfrak{y}}\end{Bmatrix},\\
&\begin{Bmatrix}\gamma_{\mathfrak{y}\mathfrak{z}}\\ \gamma_{\mathfrak{x}\mathfrak{z}}\end{Bmatrix} = \begin{Bmatrix}\gamma^0_{\mathfrak{y}\mathfrak{z}}\\ \gamma^0_{\mathfrak{x}\mathfrak{z}}\end{Bmatrix},
\end{aligned}
\tag{3}
$$

the first derivative concerning $\mathfrak{z}$ and

$$
\begin{aligned}
&\varepsilon^0_{\mathfrak{x}} = \frac{\partial \mathfrak{u}_0}{\partial \mathfrak{x}}, \qquad \varepsilon^1_{\mathfrak{x}} = \frac{\partial \mathfrak{u}_1}{\partial \mathfrak{x}}, \qquad \varepsilon^0_{\mathfrak{x}} = \frac{\partial \mathfrak{u}_0}{\partial \mathfrak{x}} + \frac{1}{2}\left(\frac{\partial \mathfrak{w}_0}{\partial \mathfrak{x}}\right)^2,\\
&\varepsilon^0_{\mathfrak{y}} = \frac{\partial \mathfrak{v}_0}{\partial \mathfrak{y}} + \frac{1}{2}\left(\frac{\partial \mathfrak{w}_0}{\partial \mathfrak{y}}\right)^2, \qquad \varepsilon^1_{\mathfrak{y}} = \frac{\partial \mathfrak{v}_1}{\partial \mathfrak{y}},\\
&\gamma^0_{\mathfrak{x}\mathfrak{y}} = \frac{\partial \mathfrak{u}_0}{\partial \mathfrak{y}} + \frac{\partial \mathfrak{v}_0}{\partial \mathfrak{x}} + \frac{\partial \mathfrak{w}_0}{\partial \mathfrak{y}}\frac{\partial \mathfrak{w}_0}{\partial \mathfrak{x}}, \qquad \gamma^1_{\mathfrak{x}\mathfrak{y}} = \frac{\partial \mathfrak{u}_1}{\partial \mathfrak{y}} + \frac{\partial \mathfrak{v}_1}{\partial \mathfrak{x}},\\
&\gamma^0_{\mathfrak{x}\mathfrak{z}} = \mathfrak{u}_1 + \frac{\partial \mathfrak{w}_0}{\partial \mathfrak{y}}, \qquad \gamma^0_{\mathfrak{y}\mathfrak{z}} = \mathfrak{u}_1 + \frac{\partial \mathfrak{w}_0}{\partial \mathfrak{x}}.
\end{aligned}
\tag{4}
$$

3.1 Electric potential distribution

The FGP porous plate can be activated by an externally applied electric voltage through electrodes attached to its top and bottom surfaces. In accordance with Maxwell's equations, the electric potential function for smart plates is represented as a combination of a half-cosine and linear variation (Komijani *et al.* 2014)

$$
\Phi(\mathfrak{x},\mathfrak{y},\mathfrak{z},\mathrm{t}) = -\cos\left(\frac{\pi}{h}\mathfrak{z}\right)\varphi(\mathfrak{x},\mathfrak{y},\mathrm{t}) + 2\frac{\mathfrak{z}}{h}V_0. \tag{5}
$$

where φ is the inner plane electric potential and V_0 is the applied electric voltage.

3.2 Constitutive equations

The relationships between stress and strain constituents of the FGP plate are presented as

$$
\begin{Bmatrix}\sigma^p\\ \boldsymbol{D}\end{Bmatrix} = \begin{bmatrix}\mathbf{C^p} & -\mathbf{e}^T\\ \mathbf{e} & \Xi\end{bmatrix}\begin{Bmatrix}\varepsilon\\ \boldsymbol{E}\end{Bmatrix}, \tag{6}
$$

In Eq. (6), $\mathbf{C^p}$ represents the elastic constant matrix for the piezoelectric layers, Ξ is the dielectric permittivity constant matrix, and $\mathbf{e}$ denotes the electromechanical coupling matrix. Their definitions are as follows

$$
\begin{aligned}
\mathbf{C^p} &= \begin{bmatrix}\overline{\mathbb{C}}_{11} & \overline{\mathbb{C}}_{12} & 0 & 0 & 0\\ \overline{\mathbb{C}}_{12} & \overline{\mathbb{C}}_{22} & 0 & 0 & 0\\ 0 & 0 & \overline{\mathbb{C}}_{66} & 0 & 0\\ 0 & 0 & 0 & \mathbb{C}_{44} & 0\\ 0 & 0 & 0 & 0 & \mathbb{C}_{55}\end{bmatrix},\\
\mathbf{e} &= \begin{bmatrix}0 & 0 & 0 & \mathbb{e}_{15} & 0\\ 0 & 0 & \mathbb{e}_{15} & 0 & 0\\ \overline{\mathbb{e}}_{31} & \overline{\mathbb{e}}_{31} & 0 & 0 & 0\end{bmatrix},\\
\Xi &= \begin{bmatrix}\Xi_{11} & 0 & 0\\ 0 & \Xi_{22} & 0\\ 0 & 0 & \overline{\Xi}_{33}\end{bmatrix}.
\end{aligned}
\tag{7}
$$

Elastic matrix components related to piezoelectric material are presented as

$$
\begin{aligned}
&\overline{\mathbb{C}}_{11} = \overline{\mathbb{C}}_{22} = \mathbb{C}_{11} - \frac{\mathbb{C}_{13}\mathbb{C}_{13}}{\mathbb{C}_{33}},\\
&\overline{\mathbb{C}}_{12} = \mathbb{C}_{12} - \frac{\mathbb{C}_{13}\mathbb{C}_{13}}{\mathbb{C}_{33}}, \qquad \overline{\mathbb{C}}_{66} = \frac{1}{2}\left(\overline{\mathbb{C}}_{11} - \overline{\mathbb{C}}_{12}\right),\\
&\overline{\mathbb{e}}_{31} = \mathbb{e}_{31} - \frac{\mathbb{C}_{13}}{\mathbb{C}_{33}}\mathbb{e}_{33}, \qquad \overline{\Xi}_{33} = \Xi_{33} + \frac{\mathbb{e}^2_{33}}{\mathbb{C}_{33}},
\end{aligned}
\tag{8}
$$

Also, $\sigma^{\mathbf{p}}$, $\mathbf{E}$ and $\mathbf{D}$ represent the stress field in piezoelectric layers compatible with the condition of absence of $\sigma^p_{\mathfrak{z}\mathfrak{z}}$, the electrical field and the electrical displacement field, respectively, and may be written as

$$
\begin{aligned}
\boldsymbol{\sigma}^p &= \left[\sigma^p_{\mathfrak{x}\mathfrak{x}},\ \sigma^p_{\mathfrak{y}\mathfrak{y}},\ \sigma^p_{\mathfrak{x}\mathfrak{y}},\ \sigma^p_{\mathfrak{y}\mathfrak{z}},\ \sigma^p_{\mathfrak{x}\mathfrak{z}}\right]^T,\\
\mathbf{D} &= \left[D_{\mathfrak{x}},\ D_{\mathfrak{y}},\ D_{\mathfrak{z}}\right]^T,\\
\mathbf{E} &= \left[E_{\mathfrak{x}},\ E_{\mathfrak{y}},\ E_{\mathfrak{z}}\right]^T = -\left[\Phi_{,\mathfrak{x}},\ \Phi_{,\mathfrak{y}},\ \Phi_{,\mathfrak{z}}\right]^T.
\end{aligned}
\tag{9}
$$

3.3 Hamilton's principle

The governing equations are derived using Hamilton's principle, which is expressed in the following form for the specific case at hand (Reddy 2003)

$$
\int_0^{\mathrm{t}} \left(\delta U - \left(\delta T + \delta W_1 + \delta W_2\right)\right)\mathrm{dt} = 0, \tag{10}
$$

The variation of strain energy of the current analysis is given by

$$\delta U=\int_V\left(\sigma_i\delta\varepsilon_i+\tau_{ij}\delta\gamma_{ij}-D_i\delta E_i\right)dV=\int_V\left[\sigma_\mathfrak{x}\delta\varepsilon_\mathfrak{x}+\sigma_\mathfrak{y}\delta\varepsilon_\mathfrak{y}+\tau_{\mathfrak{y}\mathfrak{z}}\delta\gamma_{\mathfrak{y}\mathfrak{z}}+\tau_{\mathfrak{x}\mathfrak{z}}\delta\gamma_{\mathfrak{x}\mathfrak{z}}+\tau_{\mathfrak{x}\mathfrak{y}}\delta\gamma_{\mathfrak{x}\mathfrak{y}}-D_\mathfrak{x}\delta E_\mathfrak{x}-D_\mathfrak{y}\delta E_\mathfrak{y}-D_\mathfrak{z}\delta E_\mathfrak{z}\right]dV. \quad (11)$$

The variation of kinetic energy of the current analysis is given by

$$\delta T=\int_V\left\{\rho(\mathfrak{z})\left\{\left(\frac{\partial\mathfrak{u}}{\partial\mathfrak{t}}\frac{\partial\delta\mathfrak{u}}{\partial\mathfrak{t}}+\frac{\partial\mathfrak{v}}{\partial\mathfrak{t}}\frac{\partial\delta\mathfrak{v}}{\partial\mathfrak{t}}+\frac{\partial\mathfrak{w}}{\partial\mathfrak{t}}\frac{\partial\delta\mathfrak{w}}{\partial\mathfrak{t}}\right)\right\}\right\}dV, \quad (12)$$

Substituting δU, δV, δW_1, and δW_2 in the Eq. (10), integrating through the thickness, integrating by parts with respect to $\mathfrak{x}$ and $\mathfrak{y}$, and collecting the coefficients of $\delta\mathfrak{u}_0$, $\delta\mathfrak{u}_1$, $\delta\mathfrak{v}_0$, $\delta\mathfrak{v}_1$, and $\mathfrak{w}_0$ the following governing equations are obtained

$$\begin{aligned}
&\delta\mathfrak{u}_0: && \frac{\partial\mathfrak{n}_{\mathfrak{x}\mathfrak{x}}}{\partial\mathfrak{x}}+\frac{\partial\mathfrak{n}_{\mathfrak{x}\mathfrak{y}}}{\partial\mathfrak{y}}=\mathfrak{g}_0\ddot{\mathfrak{u}}_0+\mathfrak{g}_1\ddot{\mathfrak{u}}_1, \qquad \delta\mathfrak{v}_0:\ \frac{\partial\mathfrak{n}_{\mathfrak{x}\mathfrak{y}}}{\partial\mathfrak{x}}+\frac{\partial\mathfrak{n}_{\mathfrak{y}\mathfrak{y}}}{\partial\mathfrak{y}}=\mathfrak{g}_0\ddot{\mathfrak{v}}_0+\mathfrak{g}_1\ddot{\mathfrak{v}}_1,\\
&\delta\mathfrak{w}_0: && \frac{\partial\mathfrak{q}_{\mathfrak{x}\mathfrak{z}}}{\partial\mathfrak{x}}+\frac{\partial\mathfrak{q}_{\mathfrak{y}\mathfrak{z}}}{\partial\mathfrak{y}}+\frac{\partial}{\partial\mathfrak{x}}\left(\mathfrak{n}_{\mathfrak{x}\mathfrak{x}}\frac{\partial\mathfrak{w}_0}{\partial\mathfrak{x}}\right)+\frac{\partial}{\partial\mathfrak{y}}\left(\mathfrak{n}_{\mathfrak{y}\mathfrak{y}}\frac{\partial\mathfrak{w}_0}{\partial\mathfrak{y}}\right)+\frac{\partial}{\partial\mathfrak{x}}\left(\mathfrak{n}_{\mathfrak{x}\mathfrak{y}}\frac{\partial\mathfrak{w}_0}{\partial\mathfrak{y}}\right)+\frac{\partial}{\partial\mathfrak{y}}\left(\mathfrak{n}_{\mathfrak{x}\mathfrak{y}}\frac{\partial\mathfrak{w}_0}{\partial\mathfrak{x}}\right)=\mathfrak{g}_0\ddot{\mathfrak{w}}_0,\\
&\delta\mathfrak{u}_1: && \frac{\partial\mathfrak{m}_{\mathfrak{x}\mathfrak{x}}}{\partial\mathfrak{x}}+\frac{\partial\mathfrak{m}_{\mathfrak{x}\mathfrak{y}}}{\partial\mathfrak{y}}-\mathfrak{q}_{\mathfrak{x}\mathfrak{z}}=\mathfrak{g}_1\ddot{\mathfrak{u}}_0+\mathfrak{g}_2\ddot{\mathfrak{u}}_1, \qquad \delta\mathfrak{v}_1:\ \frac{\partial\mathfrak{m}_{\mathfrak{x}\mathfrak{y}}}{\partial\mathfrak{x}}+\frac{\partial\mathfrak{m}_{\mathfrak{y}\mathfrak{y}}}{\partial\mathfrak{y}}-\mathfrak{q}_{\mathfrak{y}\mathfrak{z}}=\mathfrak{g}_1\ddot{\mathfrak{v}}_0+\mathfrak{g}_2\ddot{\mathfrak{v}}_1,\\
&\delta\varphi: && \int_{-\frac{h}{2}}^{\frac{h}{2}}\left[cos\left(\frac{\pi}{h}\mathfrak{z}\right)\left(\frac{\partial D_\mathfrak{x}}{\partial\mathfrak{x}}+\frac{\partial D_\mathfrak{y}}{\partial\mathfrak{y}}\right)+\frac{\pi}{h}sin\left(\frac{\pi}{h}\mathfrak{z}\right)D_\mathfrak{z}\right]d\mathfrak{z}=0.
\end{aligned} \quad (13)$$

The boundary conditions are defined as

$$\delta\mathfrak{u}_0=0 \quad \text{or} \quad n_\mathfrak{x}\mathfrak{n}_{\mathfrak{x}\mathfrak{x}}+n_\mathfrak{y}\mathfrak{n}_{\mathfrak{x}\mathfrak{y}}=0, \quad (14a)$$

$$\delta\mathfrak{v}_0=0 \quad \text{or} \quad n_\mathfrak{x}\mathfrak{n}_{\mathfrak{x}\mathfrak{y}}+n_\mathfrak{y}\mathfrak{n}_{\mathfrak{y}\mathfrak{y}}=0, \quad (14b)$$

$$\begin{aligned}&\delta\mathfrak{w}_0=0 \quad \text{or}\\ &n_\mathfrak{x}\left(\mathfrak{q}_{\mathfrak{x}\mathfrak{z}}+\mathfrak{n}_{\mathfrak{x}\mathfrak{x}}\frac{\partial\mathfrak{w}_0}{\partial\mathfrak{x}}+\mathfrak{n}_{\mathfrak{x}\mathfrak{y}}\frac{\partial\mathfrak{w}_0}{\partial\mathfrak{y}}\right)\\ &+n_\mathfrak{y}\left(\mathfrak{q}_{\mathfrak{y}\mathfrak{z}}+\mathfrak{n}_{\mathfrak{y}\mathfrak{y}}\frac{\partial\mathfrak{w}_0}{\partial\mathfrak{y}}+\mathfrak{n}_{\mathfrak{x}\mathfrak{y}}\frac{\partial\mathfrak{w}_0}{\partial\mathfrak{x}}\right)=0,\end{aligned} \quad (14c)$$

$$\delta\mathfrak{u}_1=0 \quad \text{or} \quad n_\mathfrak{x}\mathfrak{m}_{\mathfrak{x}\mathfrak{x}}+n_\mathfrak{y}\mathfrak{m}_{\mathfrak{x}\mathfrak{y}}=0, \quad (14d)$$

$$\delta\mathfrak{v}_1=0 \quad \text{or} \quad n_\mathfrak{x}\mathfrak{m}_{\mathfrak{x}\mathfrak{y}}+n_\mathfrak{y}\mathfrak{m}_{\mathfrak{y}\mathfrak{y}}=0, \quad (14e)$$

$$\begin{aligned}&\delta\varphi=0 \quad \text{or}\\ &n_\mathfrak{x}\left(D_\mathfrak{x}cos\left(\frac{\pi}{h}\mathfrak{z}\right)\right)+n_\mathfrak{y}\left(D_\mathfrak{y}cos\left(\frac{\pi}{h}\mathfrak{z}\right)\right)=0,\end{aligned} \quad (14f)$$

where $(n_\mathfrak{x},n_\mathfrak{y})$ denotes the unit normal-to-boundary vector.

In Eqs. (13a)-(13f), and Eqs. (14a)-(14f), we have

$$\begin{Bmatrix}\mathfrak{n}_{\mathfrak{x}\mathfrak{x}}\\ \mathfrak{n}_{\mathfrak{y}\mathfrak{y}}\\ \mathfrak{n}_{\mathfrak{x}\mathfrak{y}}\end{Bmatrix}=\int_{-h/2}^{h/2}\begin{Bmatrix}\sigma_{\mathfrak{x}\mathfrak{x}}\\ \sigma_{\mathfrak{y}\mathfrak{y}}\\ \sigma_{\mathfrak{x}\mathfrak{y}}\end{Bmatrix}d\mathfrak{z}, \quad \begin{Bmatrix}\mathfrak{q}_{\mathfrak{x}\mathfrak{z}}\\ \mathfrak{q}_{\mathfrak{y}\mathfrak{z}}\\ \mathfrak{q}_{\mathfrak{z}\mathfrak{z}}\end{Bmatrix}=\int_{-h/2}^{h/2}\begin{Bmatrix}\tau_{\mathfrak{x}\mathfrak{z}}\\ \tau_{\mathfrak{y}\mathfrak{z}}\\ \sigma_{\mathfrak{z}\mathfrak{z}}\end{Bmatrix}d\mathfrak{z}, \quad (15a)$$

$$\begin{Bmatrix}\mathfrak{m}_{\mathfrak{x}\mathfrak{x}}\\ \mathfrak{m}_{\mathfrak{y}\mathfrak{y}}\\ \mathfrak{m}_{\mathfrak{x}\mathfrak{y}}\end{Bmatrix}=\int_{-h/2}^{h/2}\mathfrak{z}\begin{Bmatrix}\sigma_{\mathfrak{x}\mathfrak{x}}\\ \sigma_{\mathfrak{y}\mathfrak{y}}\\ \tau_{\mathfrak{x}\mathfrak{y}}\end{Bmatrix}d\mathfrak{z}, \begin{Bmatrix}\mathfrak{m}_{\mathfrak{x}\mathfrak{z}}\\ \mathfrak{m}_{\mathfrak{y}\mathfrak{z}}\\ \mathfrak{m}_{\mathfrak{z}\mathfrak{z}}\end{Bmatrix}=\int_{-h/2}^{h/2}\mathfrak{z}\begin{Bmatrix}\tau_{\mathfrak{x}\mathfrak{z}}\\ \tau_{\mathfrak{y}\mathfrak{z}}\\ \sigma_{\mathfrak{z}\mathfrak{z}}\end{Bmatrix}d\,\mathfrak{z}, \quad (15b)$$

$$\mathfrak{g}_i=\int_{-h/2}^{h/2}\rho(\mathfrak{z})\,\mathfrak{z}^i d\mathfrak{z}. \qquad i=0,1,2 \quad (15c)$$

3.4 Limitations, simplifications and assumptions

For the sake of simplicity, the study establishes idealized boundary conditions and constant material properties, which do not reflect how piezoelectric materials vary in real-life applications. The changes due to manufacturing defects, material degradation, or things like temperature, are not modeled in this study. The simulations use simple models that consider the interaction of porosity and the electric fields created by the piezoelectric material, whereas lightning strikes can generate a few behaviors that may not be captured when modeling these smart structures. The study also implements the Von-Karman nondimensionalization, or the Hamiltonian principle of minimization, both of which introduce some approximations in the dynamic behavior of the smart structure, especially empirical noise in the dataset, which could limit the translations of this work to the real world.

4. Solution procedure

The core idea behind the differential quadrature method (DQ) and the higher-order differential quadrature method (HDQM) is to approximate the partial derivatives of a function with respect to a spatial variable at any discrete point, using a weighted linear combination of the function values at all chosen discrete points within the solution domain of that variable. The DQM and HDQM approximations can be effectively demonstrated with a one-dimensional function. The $\mathfrak{p}^{th}$ derivative of a function $\mathfrak{f}(\mathfrak{x})$ can be estimated using these methods.

$$\frac{\partial^\mathfrak{p}\mathfrak{f}(\mathfrak{x})}{\partial\mathfrak{x}^\mathfrak{p}}=\sum_{\mathfrak{j}=1}^{\mathbb{N}_\mathfrak{x}}\mathfrak{a}_{\mathfrak{i}\mathfrak{j}}^{(\mathfrak{p})}\mathfrak{f}(\mathfrak{x}_\mathfrak{j}), \quad \mathfrak{i}=1,2,\dots,\mathfrak{N}_\mathfrak{x} \quad \text{and} \quad \mathfrak{p}=1,2,\dots,\mathfrak{N}_\mathfrak{x}-1 \quad (16)$$

$\mathfrak{N}_\mathfrak{x}$ represents the number of discrete points selected within the solution domain. The notation $\mathfrak{a}_{\mathfrak{ij}}^{(\mathfrak{p})}$ refers to the weighting coefficients (where $\mathfrak{j} = 1,2,\dots,\mathfrak{N}_{\mathfrak{x}}$) at the ith location within the solution domain. This approximation converts a partial differential equation into a system of algebraic equations. Eq. (19) clearly highlights that a key element of the DQM and HDQM approximations is the calculation of the weighting coefficients. The procedures for determining these coefficients for both methods are outlined below.

4.1 Differential quadrature method

According to the DQM, the weighting coefficients $\mathfrak{a}_{\mathfrak{ij}}^{(\mathfrak{p})}$ for $\mathfrak{i} \neq \mathfrak{j}$ can be obtained using the following recurrence formula

$$\mathfrak{a}_{\mathfrak{ij}}^{(\mathfrak{p})} = \mathfrak{p}\left(\mathfrak{a}_{\mathfrak{ii}}^{(\mathfrak{p}-1)}\mathfrak{a}_{\mathfrak{ij}}^{(1)} - \frac{\mathfrak{a}_{\mathfrak{ij}}^{(\mathfrak{p}-1)}}{\mathfrak{x}_{\mathfrak{i}} - \mathfrak{x}_{\mathfrak{j}}}\right), \qquad (17)$$
$$\mathfrak{p} = 2,3,\dots,\mathfrak{N}_{\mathfrak{x}} - 1 \quad \text{and} \quad \mathfrak{i},\mathfrak{j} = 1,2,\dots,\mathfrak{N}_{\mathfrak{x}}.$$

where $\mathfrak{a}_{\mathfrak{ij}}^{(1)}$ is given as

$$\mathfrak{a}_{\mathfrak{ij}}^{(1)} = \frac{\mathfrak{M}^{(1)}(\mathfrak{x}_{\mathfrak{i}})}{(\mathfrak{x}_{\mathfrak{i}} - \mathfrak{x}_{\mathfrak{j}})\mathfrak{M}^{(1)}(\mathfrak{x}_{\mathfrak{j}})}, \quad \mathfrak{i},\mathfrak{j} = 1,2,\dots,\mathfrak{N}_{\mathfrak{x}}. \qquad (18)$$

The weighting coefficients when $\mathfrak{i} = \mathfrak{j}$ are given as

$$\mathfrak{a}_{\mathfrak{ii}}^{(\mathfrak{p})} = -\sum_{\mathfrak{j}=1,\mathfrak{j}\neq\mathfrak{i}}^{\mathfrak{N}_{\mathfrak{x}}} \mathfrak{a}_{\mathfrak{ij}}^{(\mathfrak{p})}, \quad \mathfrak{i} = 2,3,\dots,\mathfrak{N}_{\mathfrak{x}} \qquad (19)$$
$$\textit{and} \quad \mathfrak{p} = 1,2,\dots,\mathfrak{N}_{\mathfrak{x}} - 1.$$

In Eq. (18), $\mathfrak{M}^{(1)}$ is denoted by the following expression

$$\mathfrak{M}^{(1)}(\mathfrak{x}_k) = -\sum_{\mathfrak{j}=1,\mathfrak{j}\neq k}^{\mathfrak{N}_{\mathfrak{x}}} (\mathfrak{x}_k - \mathfrak{x}_{\mathfrak{j}}), \quad k = 1,2,3,\dots,\mathfrak{N}_{\mathfrak{x}}. \qquad (20)$$

4.2 Harmonic differential quadrature method

The weighting coefficients for the first-order derivatives $\mathfrak{a}_{\mathfrak{ij}}^{(1)}$ for $\mathfrak{i} \neq \mathfrak{j}$ can be obtained using the following formula

$$\mathfrak{a}_{\mathfrak{ij}}^{(1)} = \frac{\pi\mathfrak{T}(\mathfrak{x}_{\mathfrak{i}})}{2\mathfrak{T}(\mathfrak{x}_{\mathfrak{j}})\, sin\left[(\mathfrak{x}_{\mathfrak{i}} - \mathfrak{x}_{\mathfrak{j}})/2\pi\right]}, \quad \mathfrak{i},\mathfrak{j} = 1,2,\dots,\mathfrak{N}_{\mathfrak{x}}. \qquad (21)$$

where

$$\mathfrak{T}(\mathfrak{x}_{\mathfrak{i}}) = -\sum_{\mathfrak{j}=1,\mathfrak{j}\neq\mathfrak{i}}^{\mathfrak{N}_{\mathfrak{x}}} sin\left(\frac{\pi(\mathfrak{x}_{\mathfrak{i}} - \mathfrak{x}_{\mathfrak{j}})}{2}\right), \quad \mathfrak{j} = 1,2,3,\dots,\mathfrak{N}_{\mathfrak{x}}. \qquad (22)$$

The weighting coefficients of the first-order derivatives $\mathfrak{a}_{\mathfrak{ij}}^{(1)}$ for $\mathfrak{i} = \mathfrak{j}$ are given as

$$\mathfrak{a}_{\mathfrak{ii}}^{(1)} = -\sum_{\mathfrak{j}=1,\mathfrak{j}\neq\mathfrak{i}}^{\mathfrak{N}_{\mathfrak{x}}} \mathfrak{a}_{\mathfrak{ij}}^{(1)}, \quad \mathfrak{i} = 1,2,3,\dots,\mathfrak{N}_{\mathfrak{x}}. \qquad (23)$$

The weighting coefficients of the second-order derivatives $\mathfrak{a}_{\mathfrak{ij}}^{(2)}$ for $\mathfrak{i} \neq \mathfrak{j}$ can be obtained using the following formula

$$\mathfrak{a}_{\mathfrak{ij}}^{(2)} = \mathfrak{a}_{\mathfrak{ij}}^{(1)}\left(2\mathfrak{a}_{\mathfrak{ij}}^{(1)} - \pi ctg\left(\frac{\mathfrak{x}_{\mathfrak{i}} - \mathfrak{x}_{\mathfrak{j}}}{2} \times \pi\right)\right), \qquad (24)$$
$$\mathfrak{i},\mathfrak{j} = 1,2,3,\dots,\mathfrak{N}_{\mathfrak{x}}.$$

The weighting coefficients of the second-order derivatives $\mathfrak{a}_{\mathfrak{ij}}^{(2)}$ for $\mathfrak{i} = \mathfrak{j}$ are given as

$$\mathfrak{a}_{\mathfrak{ii}}^{(2)} = -\sum_{\mathfrak{j}=1,\mathfrak{j}\neq\mathfrak{i}}^{\mathfrak{N}_{\mathfrak{x}}} \mathfrak{a}_{\mathfrak{ij}}^{(2)}, \quad \mathfrak{i} = 1,2,3,\dots,\mathfrak{N}_{\mathfrak{x}}. \qquad (25)$$

4.3 Two-dimensional approximation

The three-dimensional approximations using DQM and HDQM can be easily extended from the one-dimensional case. For a two-dimensional unknown function $\mathfrak{f}\,(\mathfrak{x},\mathfrak{y})$, the approximations are derived from the following expressions

$$\frac{\partial\mathfrak{f}}{\partial\mathfrak{x}}\Big|_{\mathfrak{x}=\mathfrak{x}_{\mathfrak{i}},\,\mathfrak{y}=\mathfrak{y}_{\mathfrak{j}}} = \sum_{\mathfrak{p}=1}^{\mathfrak{N}_{\mathfrak{x}}}\sum_{k=1}^{\mathfrak{N}_{\mathfrak{y}}} \mathfrak{a}_{\mathfrak{ip}}^{\mathfrak{x}} I_{\mathfrak{p}k}^{\mathfrak{y}} \mathfrak{f}_{k\mathfrak{j}}, \qquad (26a)$$

$$\frac{\partial\mathfrak{f}}{\partial\mathfrak{y}}\Big|_{\mathfrak{x}=\mathfrak{x}_{\mathfrak{i}},\,\mathfrak{y}=\mathfrak{y}_{\mathfrak{j}}} = \sum_{\mathfrak{p}=1}^{\mathfrak{N}_{\mathfrak{x}}}\sum_{k=1}^{\mathfrak{N}_{\mathfrak{y}}} I_{\mathfrak{ip}}^{\mathfrak{x}} \mathfrak{a}_{\mathfrak{p}k}^{\mathfrak{y}} \mathfrak{f}_{k\mathfrak{j}}, \qquad (26b)$$

$$\frac{\partial}{\partial\mathfrak{x}}\left(\frac{\partial\mathfrak{f}}{\partial\mathfrak{y}}\Big|_{\mathfrak{x}=\mathfrak{x}_{\mathfrak{i}},\,\mathfrak{y}=\mathfrak{y}_{\mathfrak{j}}}\right) = \sum_{\mathfrak{p}=1}^{\mathfrak{N}_{\mathfrak{x}}}\sum_{k=1}^{\mathfrak{N}_{\mathfrak{y}}} \mathfrak{a}_{\mathfrak{ip}}^{\mathfrak{x}} \mathfrak{a}_{\mathfrak{p}k}^{\mathfrak{y}} \mathfrak{f}_{k\mathfrak{j}}, \qquad (26c)$$

$$\frac{\partial^2\mathfrak{f}}{\partial\mathfrak{x}^2}\Big|_{\mathfrak{x}=\mathfrak{x}_{\mathfrak{i}},\,\mathfrak{y}=\mathfrak{y}_{\mathfrak{j}}} = \sum_{\mathfrak{p}=1}^{\mathfrak{N}_{\mathfrak{x}}}\sum_{k=1}^{\mathfrak{N}_{\mathfrak{y}}} \mathbb{B}_{\mathfrak{ip}}^{\mathfrak{x}} I_{\mathfrak{p}k}^{\mathfrak{y}} \mathfrak{f}_{k\mathfrak{j}}, \qquad (26d)$$

$$\frac{\partial^2\mathfrak{f}}{\partial\mathfrak{y}^2}\Big|_{\mathfrak{x}=\mathfrak{x}_{\mathfrak{i}},\,\mathfrak{y}=\mathfrak{y}_{\mathfrak{j}}} = \sum_{\mathfrak{p}=1}^{\mathfrak{N}_{\mathfrak{x}}}\sum_{k=1}^{\mathfrak{N}_{\mathfrak{y}}} I_{\mathfrak{ip}}^{\mathfrak{x}} \mathbb{B}_{\mathfrak{p}k}^{\mathfrak{y}} \mathfrak{f}_{k\mathfrak{j}}, \qquad (26e)$$

$\mathfrak{a}_{\mathfrak{ip}}^{\mathfrak{x}}$, $\mathfrak{a}_{\mathfrak{p}k}^{\mathfrak{y}}$, $\mathbb{B}_{\mathfrak{ip}}^{\mathfrak{x}}$, and $\mathbb{B}_{\mathfrak{p}k}^{\mathfrak{y}}$ represent the weighting coefficients for the $\mathfrak{p}^{th}$ partial derivatives of the function at the point $(\mathfrak{i},\mathfrak{j})$ along the $\mathfrak{x}$, and $\mathfrak{y}$ directions, respectively. Meanwhile, $\mathfrak{N}_{\mathfrak{x}}$, and $\mathfrak{N}_{\mathfrak{y}}$ denote the total number of discrete points selected along the $\mathfrak{x}$, and $\mathfrak{y}$-axes. The parameters $I_{\mathfrak{ip}}^{\mathfrak{x}}$, $I_{\mathfrak{p}k}^{\mathfrak{y}}$, $I_{\mathfrak{ip}}^{\mathfrak{x}}$, and $I_{\mathfrak{p}k}^{\mathfrak{y}}$ refer to the identity matrix. In addition to utilizing Chebyshev polynomial grid points, the seed points may be distributed along the $\mathfrak{x}$ and $\mathfrak{y}$ directions as follows

$$\mathfrak{x}_{\mathfrak{i}} = \frac{a}{2}\left(1 - \cos\left(\frac{(\mathfrak{i}-1)}{(\mathfrak{N}_{\mathfrak{x}} - 1)}\pi\right)\right), \qquad (27a)$$
$$\mathfrak{i} = 1,2,3,\dots,\mathfrak{N}_{\mathfrak{x}},$$

$$\mathfrak{y}_{\mathfrak{j}} = \frac{b}{2}\left(1 - \cos\left(\frac{(\mathfrak{j}-1)}{(\mathfrak{N}_{\mathfrak{y}} - 1)}\pi\right)\right), \qquad (27b)$$
$$\mathfrak{j} = 1,2,3,\dots,\mathfrak{N}_{\mathfrak{y}},$$

Before applying the HDQM for free vibration analysis, the displacement variables need to be modified to incorporate the frequency and time parameters, as follows

$$\begin{aligned}
\mathfrak{u}_0(\mathfrak{x},\mathfrak{y},\mathfrak{t}) &= \bar{\mathfrak{u}}_0(\mathfrak{x},\mathfrak{y})e^{i\omega\mathfrak{t}},\\
\mathfrak{v}_0(\mathfrak{x},\mathfrak{y},\mathfrak{t}) &= \bar{\mathfrak{v}}_0(\mathfrak{x},\mathfrak{y})e^{i\omega\mathfrak{t}},\\
\mathfrak{w}_0(\mathfrak{x},\mathfrak{y},\mathfrak{t}) &= \bar{\mathfrak{w}}_0(\mathfrak{x},\mathfrak{y})e^{i\omega\mathfrak{t}}.\\
\mathfrak{u}_1(\mathfrak{x},\mathfrak{y},\mathfrak{t}) &= \bar{\mathfrak{u}}_1(\mathfrak{x},\mathfrak{y})e^{i\omega\mathfrak{t}},\\
\mathfrak{v}_1(\mathfrak{x},\mathfrak{y},\mathfrak{t}) &= \bar{\mathfrak{v}}_1(\mathfrak{x},\mathfrak{y})e^{i\omega\mathfrak{t}},
\end{aligned} \tag{28}$$

Here, ω represents the complex natural frequency, and i denotes $\sqrt{-1}$. As a result, the algebraic eigenvalue problem can be reformulated in matrix notation as

$$(\mathbf{K_L} + \mathbf{K_{NL1}} + \mathbf{K_{NL2}})d - \mathbf{M}\omega^2 d = 0. \tag{29a}$$

$$d = [\bar{\mathfrak{u}}_0 \;\; \bar{\mathfrak{v}}_0 \;\; \bar{\mathfrak{w}}_0 \;\; \bar{\mathfrak{u}}_1 \;\; \bar{\mathfrak{v}}_1]^T. \tag{29b}$$

In this equation, $\mathbf{K_L}$ represents the linear elastic stiffness matrix, whereas $\mathbf{K_{NL1}}$ and $\mathbf{K_{NL2}}$ are referred to as the nonlinear elastic stiffness matrices, which depend linearly and quadratically on the displacement vector, respectively. The system's vibrational frequencies are determined by solving Eq. (29a). Additionally, the dimensionless parameters can be expressed as follows

$$\omega_{NL}^{*} = \omega a\sqrt{\frac{\rho^b}{\mathbb{C}_{11}^{b}}}, \quad \Phi^{*} = \frac{V_0}{10^2}. \tag{30}$$

5. Deep neural networks to model the current work via appropriate dataset of the presented mathematics simulation results

Intelligent structures have revolutionized the present-day methods of engineering. Intelligent structures obviously have "intelligent" components. This means that through the addition of intelligent "stuff," structures can react and adapt over time. The intelligent stuff that we will focus on is piezoelectrics need a quick abstraction. Piezoelectric composites are extremely effective at converting electricity into motion and vice versa; it would be hard to imagine a better material for feeling, reaction, and monitoring structural health. It is important to note that piezoelectrics can likewise have material and physical degradation. Various issues, such as small porosity, can arise from fatigue or overload and can hinder the performance of the system. Certainly, monitoring the structural condition or health of any piezoelectric system requires that we detect the presence of porosity. Notably, to ensure a smart system is safe and to perform to its capabilities it will determine the priority level of porosity detection. Conventional methods of detecting structural issues are often not able sensitive or quick enough in large complicated structures during "real-time" inspection. Thus, this research presents the combination of vibration monitoring and deep learning as a double-check for personal meaning. The overall aim was to conduct porosity detection in a smart structure involving piezoelectric materials. The way we will define and visualize the vibrational responses of the smart plates was defined with a mathematical modeling approach for our understanding of deflections and motions of bending plates and/or thick plates include higher hiring pace. Porosity are put in the piezoelectric pieces causing some and the stiffness of the structure to change which also changes the vibration response behavior characteristics of the structure. We then use the math to create an abundance of data models based on vibration response behavior characteristics of these structures with the same porosity under varying conditions. This data can now be used to train a computer program that learns based on the differences in the vibrational response with the porosity. To verify that we are able to find porosity, we can develop a special configuration whereby the computer program learns to classify the vibrations by the type of porosity or the severity of porosity. The computer learns these complex relationships to the data as they relate to the crack vibrations and is more accurate than simply following rules. The bottom line is that by combining the vibrational response behavior characteristics and machine learning we are successfully identifying porosity and potentially, even doing it in real-time so we can monitor structures. This work is part of the future for identifying smart structures using our knowledge of vibrational response behavior characteristics together with artificial intelligence to make better monitoring decisions. The results show that this mix is much better for detecting porosity in piezoelectric materials. It is faster, accurate, and can be used to monitor how structures are behaving through operation. This [proposed] concept can be adapted to a variety of smart materials and allow monitoring of systems that are important, like airplanes, buildings, and robots, without the requirement for humans to do so all of the time.

Principal formulations of the DNN algorithm:

In this article the following formulation are considered:

$X \in R^{n\times d}$: Input dataset (nonlinear vibration features; e.g., frequency response, displacement amplitude)

$Y \in R^{n\times c}$: Output labels (defect class or severity level)

f_θ: Deep neural network function parameterized by weights θ.

5.1 Input layer

$$a^{(0)} = X. \tag{31}$$

Raw features from simulation results are fed into the input layer.

5.2 Hidden layers (Dense with activation)

For each hidden layer $l = 1,2,\ldots,L$

$$a^{(l)} = \sigma\big(W^{(l)}a^{(l-1)} + b^{(l)}\big). \tag{32}$$

where σ is the activation function (e.g., ReLU), $W^{(l)}$ are weights, and $b^{(l)}$ are biases.

5.3 Output layer (Softmax for classification)

$$\hat{Y} = \vartheta\big(W^{(L+1)}a^{(L)} + b^{(L+1)}\big). \tag{33}$$

where ϑ is a softmax function for multi-class classification or identity for regression.

5.4 Loss function

For classification (cross-entropy)

$$L(\vartheta) = -\frac{1}{n}\sum_{i=1}^{n}\sum_{j=1}^{c} Y_{ij}\log\left(\hat{Y}_{ij}\right). \tag{34}$$

5.5. Optimization (Adam)

$$\theta \leftarrow \theta - \eta \nabla_\theta L(\theta). \tag{35}$$

where η is the learning rate.

6. Results and discussion

6.1 Verification

In Table 1 we provide a comparison of the frequency results of simply supported piezoelectric plates to the analysis presented in the literature (Ref. (Barati *et al.* 2017)), under BN different electric potential states and power indices (0.2, 1 and 5). The frequencies were reported pertaining to the V_0 conditions of -500, 0 and 500 respectively, highlighting the dynamic response of the plate in each given condition. For each case of V_0, it is clear that the frequency obtained from the present study was marginally different to the frequencies from the revised literature, demonstrating the efficacy of using the attribute of piezoelectricity in the proposed methodology to assess the behavior of piezoelectric materials. In considering the power index, the comparison of the three illustrative conditions has established a better understanding of how the given electric potential, alongside contributing mechanical conditions affect the material responses. The correlate levels of results produced through the two methods (present study vs. literature) validated that the proposed nonlinear method (combining Von Karman's nonlinearity, and Maxwell's equations) captures the rules of nature of a piezoelectric plate, which defines usefulness when it comes to detection of defects, as changes in frequency response demonstrate likely structural implications (i.e., to do with porosity; materially being impacted etc.), which may well provide contextual ground to judgement on the performance of smart structures. Finally, the material corroborates the method's ability to predict frequencies, giving weight to the overall approach involved in defect detection in smart structures.

6.2 Parametric results

Table 2 indicates the frequency response of the plate's vibration response. It indicates how the frequency responds to porosity (β). The table shows frequency shifts with respect to shape whereby β is between 0 and 1. As β gets larger, the frequency decreases. So it is true, porosity indeed changes how it vibrates. This table also demonstrates the porosity's affect on the strength of the plate, in that the emptier area there is, the lower the vibration frequency. This is helpful in finding material flaws because empty area comes from holes or porosity and when we look at the frequency shifts with different levels of porosity, we can see for ourselves these metrics problems. The importance of porosity and its affect on vibration is greater when we are considering whether we can use these materials in technologies such as smart buildings. This table demonstrates that porosity and material flaws do affect frequency response and help us make improvements in the way we can measure material flaws, through the use of vibrations.

Table 1 A comparison study between the frequency results of simply-supported piezoelectric plate structure via those of published article in the literature

V_0	Methods	Power index		
		0.2	1	5
-500	Present	6.14521	6.00125	5.84125
	Ref. (Barati *et al.* 2017)	6.20555	6.00294	5.85444
0	Present	6.02145	5.79812	5.65911
	Ref. (Barati *et al.* 2017)	6.03027	5.81787	5.66120
500	Present	5.81256	5.61915	5.44912
	Ref. (Barati *et al.* 2017)	5.84974	5.62671	5.46113

Table 2 The dynamic response of piezoelectric plates in terms of the normalized nonlinear frequency under different porosity conditions

β	h/a			
	0.07	0.08	0.09	0.1
1	0.4151	0.4685	0.5365	0.5891
0.75	0.3651	0.3980	0.4595	0.5112
0.5	0.3152	0.3365	0.4021	0.4451
0.25	0.2356	0.2651	0.2985	0.3548
0	0.1985	0.2152	0.2697	0.3196

The normalized nonlinear frequency and aspect ratio, for selected values of the porosity parameter, is found in Table 3, which considers geometry aspect ratios ranging from 1 to 1.3 with β values of 1, 0.75, 0.5 and 0.25. This table indicates the frequency response of a piezoelectric plate, showing the complete transition of frequency response of the piezoelectric plate and hints how the material vibrates under variable changes in the structure and material aspects. As can be expected the normalized nonlinear frequency of the piezoelectric plate decreases due to increasing aspect ratio, which means that the frequencies associated with wider plates (i.e., thinner plates) will be lower than small aspect ratio plates. This table also indicates the salient relationship between frequencies that are lowered as the result of increasing porosity, which indicates a structural response that is rooted in material defects. This table is useful in assessing the way that geometry and porosity of the plate relate to the frequency shifts, which are useful in monitoring the material's debris and anomalous defects. By measuring frequency shifts in a piezoelectric plate to characterize porosity or material anomalies, it is then possible to monitor the frequency changes that will assist in identifying isolation that may

Table 3 The relationship between the normalized nonlinear frequency and the aspect ratio for various values of the porosity parameter

β	h/a			
	1	1.1	1.2	1.3
1	0.25	0.5895	0.5012	0.4124
0.75	0.5	0.4451	0.3875	0.3324
0.5	0.75	0.3548	0.3102	0.2660
0.25	1	0.3196	0.2825	0.2471

have suffered from degradation or structural issues. The process of identifying defect areas using nonlinear vibration analysis should be more refined and targeted for material degradation.

The normalized nonlinear frequency values of differing β values and normalized electric potentials are presented in Table 4 to provide a more localized view of the combined effect of electric load and material-specific porosity. In actuality, this table is intended to highlight the frequency variations across the several β values calculated in which the normalized electric potential was measured as it varied from 0 to 0.3. When looking at the rows of data, you should also notice that porosity appears to have an overall significant effect on frequency response. The general trend illustrates that with increasing porosity, the resonant frequency decreased. This is predictable since higher porosity generally means less stiffness of that material, thus generating lower frequencies. Electric potential clearly has an effect on frequency as well but porosity appears to have a more significant effect. The values and trends presented in this table provide evidence that porosity and electric loading as a team produce the subsequent behavior of the piezoelectric plate. While we were not analyzing the resonant frequencies for changing loads or material defect directly, the identification of frequencies could be used to indicate areas of potential damage like holes or areas of porosity in the material. Additionally, if the frequency shift can be pinned down to either changes in electric loads or material with differing levels of porosity, then you have a method to locate and then evaluate damage in piezoelectric materials. In conclusion, these developments provide intriguing possibilities for monitoring the health of operational infrastructure, while also extending its usefulness as a smart material from an engineering design standpoint.

Table 4 The values of the normalized nonlinear frequency for different values of β and the normalized electric potential

β	ϕ^*			
	0	0.1	0.2	0.3
1	0.7895	0.6821	0.5795	0.4612
0.75	0.7154	0.6048	0.5074	0.3971
0.5	0.6125	0.5141	0.4332	0.3197
0.25	0.5861	0.4912	0.4131	0.2968

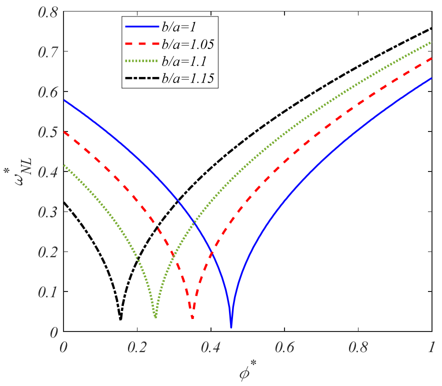

Fig. 2 The variation in the normalized nonlinear frequency as a function of the normalized electric potential for different aspect ratios in piezoelectric plates

Fig. 2 demonstrates the variations in the normalized non-linear frequency as a function of normalized electrical potential for piezoelectric plates of various aspect ratios, i.e. b/a = 1, 1.05, 1.1, and 1.15. This figure illustrates the role of these aspect ratios on the resonant frequencies of the plates. The figure shows that the curves demonstrate non-linear behavior, but that a relationship exists with the electrical potential and the frequency response of the plate, indicating that the dynamic characteristics of the material are affected by mechanical loads as well as electrical loads. The changing frequency response due to increased b/a ratios is significant towards understanding resonant characteristics due to geometry. As we can use the frequency variation to determine defects existing inside the materials, the frequency spectrum variations show that when a frequency spectrum changes, some event may be occurring in the material's structure, like getting weaker or flaws, as in micro-holes or porosity. This highlights the importance of geometry and dimension for the materials to be used while inspecting for faults in piezoelectric materials, since they undergo proportional deformations due to applied electricity in turn altering the frequency spectrum. As a result, we have a means of using special vibration analysis to monitor the health of structures to determine if there are any defects, and its most effective in cases of smart structures that have sensors on them and other devices.

In Fig. 3, we can see how a nonlinear frequency behaves with respect to how much electrical energy we impose on it. They made the numbers easy to compare by normalizing them, because there are four lines, and each line represents a different aspect ratio (h/a) that is 0.07, 0.08, 0.09, and 0.1. What the results show is as increases, the normalized nonlinear frequency goes down. An electrical potential applies an influence on how the material will move and the motion will become nonlinear. These curves illustrate that the aspect ratio is relevant to the frequency response of the system. The data indicates that smaller aspect ratios ($h/a = 0.07$) yield larger normalized frequencies while larger aspect ratios (h/a = 0.10) yield lower frequencies. Thus, thicker plates with smaller aspect ratios will be stiffer and likely vibrate at higher frequencies with an applied electrical load. This method is proving to be effective for locating flaws and defects in piezoelectric materials. When

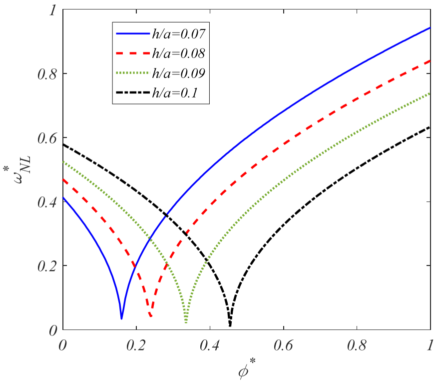

Fig. 3 The relationship between the normalized nonlinear frequency and the normalized electric potential for different values of the aspect ratio

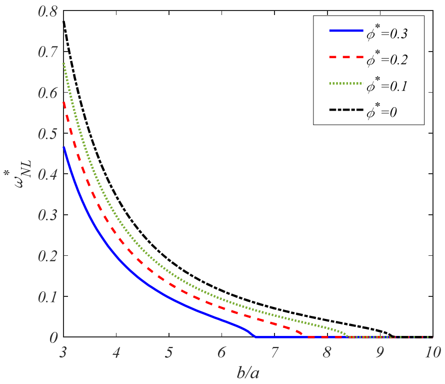

Fig. 5 The effect of the aspect ratio on the normalized nonlinear frequency for different values of the normalized electric potential

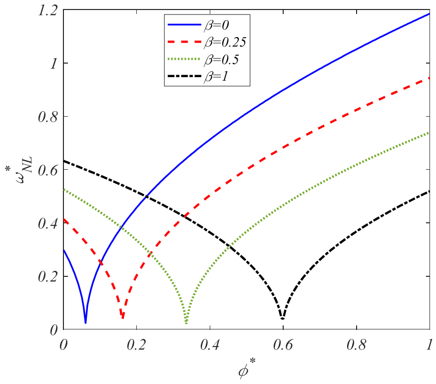

Fig. 4 The relationship between the normalized nonlinear frequency and the normalized electric potential for various porosity levels

there are defects or weaknesses, they will change how stiff something is, and how it vibrates. The change in frequency response can indicate if it is a problem as it relates to its shape and electrical charge. This knowledge of defects will help inform one's ability to maintain smart materials in better condition.

In Fig. 4, a relationship between normalized nonlinear frequency and normalized electric potential is illustrated for different levels of porosity. As ϕ^* increases, normalized nonlinear frequency decreases for the entire spectrum of β values. The actual changes are larger at higher β values. This is logical, as more porosity will reduce the stiffness of the plate, inducing a lower resonant frequency. Overall, the curves show that a plate with more porosity (i.e., β = 1) has a much lower frequency response as compared to a plate with less porosity (i.e., β = 0) under an equivalent level of electric potential. This plot information would be useful for detecting flaws in piezoelectric materials. Increased porosity can introduce failure, such as porosity or holes, which can lead to a lower stiffness of the material, in turn, causing a reduction in the resonant frequency. Thus, cutting the frequency against electric potential for various values of porosity may help detect material defects within smart structures.

Fig. 5 examines how a normalized aspect ratio affects the normalized nonlinear frequency for various normalized electric potential values ($\phi^* = 0, 0.1, 0.2, 0.3$). The graph shows as the normalized aspect ratio increases, the resonance frequency decreases, which clearly shows that geometry is pertinent to the motion of the plate. The trend shows that as the width-to-thickness (b/a) ratio increases, the normalized nonlinear frequency decreases, regardless of electric potential. The larger the plates (the higher ratio of b/a), the less stiff they become, and the lower the frequencies become. The graph demonstrates that the normalized electric potential affects the frequency response as well, where the electric potential increases the normalized aspect ratio while lowering the frequencies for the b/a ratios. Overall, this graph is very useful for understanding how geometric changes, specifically changes to the width-to-thickness ratio, impact the behavior of vibrating piezoelectric plates. Defects can certainly interfere with those geometric changes. Frequency differences could yield defect information. Structural defects or issues formulated in piezoelectric materials used for smart structures could be detected through tracking electric potential frequency changes and frequency changes as the aspect ratio increases.

Fig. 6 examines the impact of aspect ratio and porosity coefficient on the normalized nonlinear frequency of the piezoelectric plate. The plot contains curves for four values of β, showing the frequency response as b/a increases, from 3 to 10. The results indicate that the normalized nonlinear frequency decreases as b/a and β increase. The plot shows that the frequency response is decreasing for all β as aspect ratio increases. Higher values of β will produce lower values of frequency response. This is logical because higher porosity reduces the stiffness of the material, and higher aspect ratios can have less stiffness and have lower frequencies. This plot provides you useful information to assist you in finding defects in piezoelectric materials. The effect that frequency response has from porosity and aspect ratio is useful to locate defects such as porosity or voids, since these defects will change the material properties. Observing trends in frequency response with respect to porosity and a spect ratio in piezoelectric plates can help you locate issues in smart structures, assist in monitoring their structural health over time, and ultimately aid in

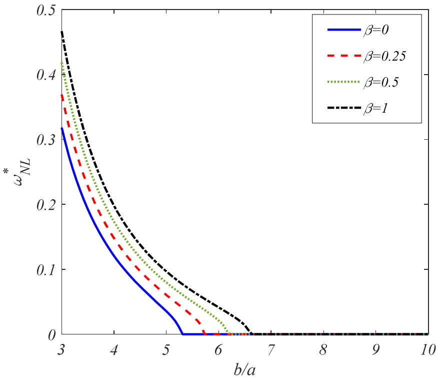

Fig. 6 The influence of the aspect ratio and porosity coefficient on the normalized nonlinear frequency of the piezoelectric plate

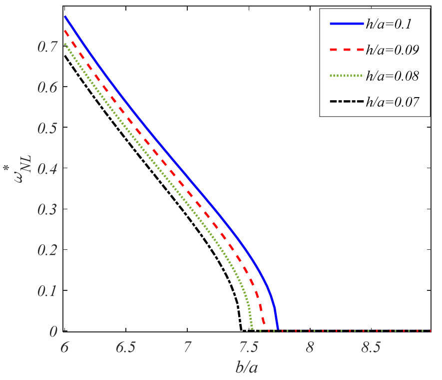

Fig. 7 The impact of the aspect ratio on the normalized nonlinear frequency for various values of the normalized electric potential

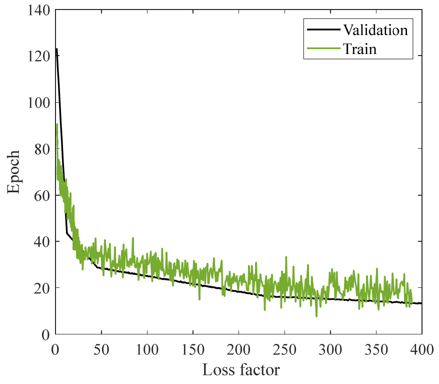

Fig. 8 The loss factor as a function of the number of epochs during training and validation for the DNN algorithm

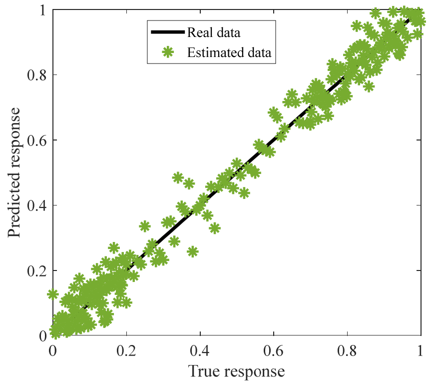

Fig. 9 The predicted response from the DNN algorithm against the true response from the real data to evaluate the model's accuracy

finding defects early.

Fig. 7 evaluates how the aspect ratio affects the normalized nonlinear frequency for different normalized values of electric potential considering different amounts of porosity (β = 0.25, β = 0.5, β = 1). The figure displays that the electric potential, porosity, and geometry affect the frequency response of the piezoelectric plate. The plot indicates that as the aspect ratio b/a increases, the normalized nonlinear frequency decreases for all β values. Porosity becomes further important at larger aspect ratios because greater porosity or β value will cause larger drops in normalized nonlinear frequencies. The plot indicates that as ϕ^* increases, the frequency response decreases independent of aspect ratio or porosity. The plot is useful for defect detection because alterations in the aspect ration and porosity of piezoelectric materials generate shifts in the frequency response. These shifts may mean the performance of the material is decreasing or there is a defect, such as porosity or pinholes. Monitoring frequency shift as a function of electric potential, geometry, and porosity allows a means of potentially detecting issues early, decreasing the chances that piezoelectric materials in smart structures are failing.

6.3 DNN results

Fig. 8 presents the change in loss factor over the number of epochs throughout training and validation for the DNN algorithm. The x-axis refers to epochs and the y-axis refers to the loss factor. The two curves show the model as it performs during training. The further the curves go down, the better the model performs and fits the data. The training curve has some variation in it, which shows that there are stages in training in which the model over-fits or is unstable. The validation curve decreases, therefore there is less fluctuation in how well the model performs in unseen data. This particular plot is extremely helpful in defining the DNN model's convergence. If the loss reduces stably through training and validation, this means the model is learning from the data. If loss is reducing with time, this means that the DNN algorithm is predicting the output accurately and the means by validating the algorithm's performance in matching the mathematical simulation.

Fig. 9 illustrates a comparison of what our DNN algorithm predicted with the actual data to see how well our model performs. The x-axis represents the real data, and the y-axis represents the predicted by model. This chart visualizes both the predictions and the model's values. This scatter plot shows the distance between the predicted points

Table 5 The presented hyperparameters of the current DNN algorithm

Hyperparameter	Value	Description
Input dimension	50	Number of features per sample
Hidden layers	3	Number of fully connected hidden layers
Units per hidden layer	128	Neurons per hidden layer
Activation function	ReLU	Applied after each dense layer
Output dimension	3	Number of classes
Output activation	Softmax (classification)	Based on task type
Loss function	MSE (regression)	Chosen depending on label format
Optimizer	Adam	Adaptive gradient descent optimizer
Learning rate	0.001	Initial step size for weight updates
Batch size	32	Number of samples per training batch
Epochs	350	Total training iterations over the dataset
Dropout rate	0.2	Prevents overfitting by randomly dropping neurons during training
Weight initialization	He Normal	Suitable for ReLU activations
Early stopping patience	10	Stops training if no improvement for 10 epochs
Validation split	0.2	Percentage of training data used for validation
Random seed	42	For reproducibility of results

and the real data points. The DNN model is highly aligned with the real data. The similarities between the predicted and actual data points is very close in nature. This suggests that there is significant viability of the DNN model when recreating real data - that it is capable of learning from the dataset to make reasonably accurate predictions. The degree to which the two data are mapped suggests that the model is learning some pattern into the data. This plot is a practical way to understand how well the DNN can predict values, and to replicate the forms that the math representation shows.

The presented hyperparameters of the current DNN algorithm is given in Table 5.

Fig. 10 compares the results of the DNN algorithm, and mathematical simulation of the normalized nonlinear frequency while varying the normalized electric potential. The x-axis is for ϕ^* while the y-axis records the normalized nonlinear frequency. The plot contains two curves. One is the output of the DNN algorithm and the other is the output of the mathematical simulation. The output of the DNN algorithm resembles the mathematical simulation and both curves follow a similar trend. As ϕ^* grows larger, the frequency decreases, which is the general behavior observed for piezoelectric materials when varying the electric potential. The fact that normalized nonlinear frequency data from the DNN is consistent with the results generated from the simulation shows that it is able to learn and can predict the nonlinear dynamic behavior of the system. The value of the current plot is for why the DNN model has a high correspondence with physical phenomena that could be used as a substitute to a mathematical simulation.

Fig. 11 compares how the DNN algorithm performs compared to a mathematical simulation worth investigating in terms of normalized nonlinear frequency and the aspect

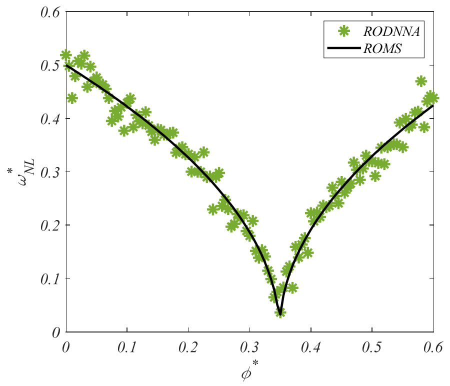

Fig. 10 The comparison between the results of the DNN algorithm and the mathematical simulation for the normalized nonlinear frequency as a function of the normalized electric potential

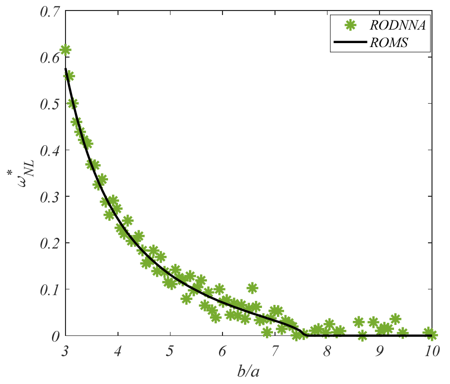

Fig. 11 The results of the DNN algorithm with the mathematical simulation for the normalized nonlinear frequency as a function of the aspect ratio of the piezoelectric plate

ratio of a piezoelectric plate. The aspect ratio is on the x-axis and the normalized nonlinear frequency is on the y-axis. The green stars are the RODNNA results and the black line indicated the ROMS results. The graph indicates that with increasing aspect ratio b/a, the normalized nonlinear frequency decreases as would be expected from piezoelectric materials. Because the predictions of the DNN are quite close to the ROMS results, this indicates that the DNN model is doing a fairly good job of picking up the nonlinearity of the system. The DNN can predict the results without lengthy mathematical simulations. This means it would lend itself reasonably well to analyzing a variety of systems based on input data that was otherwise difficult to comprehend. The better part of this graph serves as additional proof that the DNN model can learn what the behavior of piezoelectric things are likely to be based on the input data, which is a valuable resource for engineering endeavors.

7. Conclusions

In short, this work provides an excellent means of identifying defects in piezoelectric materials within smart structures, specifically FGP porous plates with an electric current. The combination of additionally phenomena characterized in this work incorporating Von-Karman nonlinearity with Maxwell's equations did a great job in representing the difficult back and forth between the mechanical and electrical systems inherent to the material. Exploring the influence of porosity in defect detection demonstrates that it can significantly influence recoverable energy of material. The use of Hamilton's rule provided an accessible means of extracting the primary equations of motion, which provides a solid foundation for studying the system once it becomes nonlinear. The use of the HDQM for integrating numerically proved to be an effective way to accurately integrate the equations of motion. This allowed for a robust dataset to be established for training DNNs for detection and classification of defects. Overall the DNN model results demonstrate that we can accurately infer detections and discuss defect classification even in complicated problems; while minimizing computational burden. Additionally, tuning the DNN's configurations improved the model even further, meaning that it can accommodate any real-world scenario personally. This research represented a significant advance to smart structural health monitoring by providing an affordable, fast way to detect flaws in piezoelectric materials. By incorporating deep learning techniques and traditional numerical methods, the research offers, the DNN will offer a new framework for future studies in smart material and structural monitoring. Overall, the framework worked out well and can be accelerated to allow for additional steps towards smart monitoring systems for futuristic engineering applications.

Acknowledgments

The authors extend their appreciation to the Deanship of Research and Graduate Studies at King Khalid University for funding this work through Large Research Project under grant number RGP.2/203/46. Also, the authors extend their appreciation to the Deanship of Scientific Research at Northern Border University, Arar, KSA for funding this research work through the project number "NBU-FFR-2025-2105-07".

References

Abbaspour, F., Arvin, H. and Shahriari-kahkeshi, M. (2022), "Nonlinear vibration control of a piezoelectric graphene sheet reinforced microplate with thermal uncertainty: feedback linearization and sliding mode approaches", *Thin-Wall. Struct.*, **181**, p. 110129. https://doi.org/10.1016/j.tws.2022.110129

Al-Furjan, M., Yang, Y., Farrokhian, A., Shen, X., Kolahchi, R. and Rajak, D.K. (2022), "Dynamic instability of nanocomposite piezoelectric-leptadenia pyrotechnica rheological elastomer-porous functionally graded materials micro viscoelastic beams at various strain gradient higher-order theories", *Polym. Compos.*, **43**(1), 282-298. https://doi.org/10.1002/pc.26570

Al-Osta, M.A., Saidi, H., Tounsi, A., Al-Dulaijan, S., Al-Zahrani, M., Sharif, A. and Tounsi, A. (2021), "Influence of porosity on the hygro-thermo-mechanical bending response of an afg ceramic-metal plates using an integral plate model", *Smart Struct. Syst., Int. J.*, **28**(4), 499-513. https://doi.org/10.12989/sss.2021.28.4.499

Alrashdan, M.H. (2020), "MEMS piezoelectric micro power harvester physical parameter optimization, simulation, and fabrication for extremely low frequency and low vibration level applications", *Microelectr. J.*, **104**, p. 104894. https://doi.org/10.1016/j.mejo.2020.104894

Alshenawy, R., Safaei, B., Sahmani, S., Elmoghazy, Y., Al-Alwan, A. and Al Nuwairan, M. (2022), "Buckling mode transition in nonlinear strain gradient-based stability behavior of axial-thermal-electrical loaded fg piezoelectric cylindrical panels at microscale", *Eng. Anal. Bound. Elem*, **141**, 36-64. https://doi.org/10.1016/j.enganabound.2022.04.022

Anitescu, C., İsmail Ateş, B. and Rabczuk, T. (2023), "Physics-informed neural networks: theory and applications", In: *Machine Learning in Modeling and Simulation: Methods and Applications*, Springer, pp. 179-218. https://doi.org/10.1007/978-3-031-36640-8_7

Arefi, M., Bidgoli, E.M.R., Dimitri, R., Bacciocchi, M. and Tornabene, F. (2018), "Application of sinusoidal shear deformation theory and physical neutral surface to analysis of functionally graded piezoelectric plate", *Compos. Part B: Eng.*, **151**, 35-50. https://doi.org/10.1016/j.compositesb.2018.06.008

Barati, M.R., Shahverdi, H. and Zenkour, A.M. (2017), "Electro-mechanical vibration of smart piezoelectric fg plates with porosities according to a refined four-variable theory", *Mech. Adv. Mater. Struct.*, **24**(12), 987-998. https://doi.org/10.1080/15376494.2016.1196773

Barooti, M.M., Safarpour, H. and Ghadiri, M. (2017), "Critical speed and free vibration analysis of spinning 3d single-walled carbon nanotubes resting on elastic foundations", *Eur. Phys. J. Plus*, **132**, 1-21. https://doi.org/10.1140/epjp/i2017-11403-3

Beni, Z.T. and Beni, Y.T. (2022), "Dynamic stability analysis of size-dependent viscoelastic/piezoelectric nano-beam", *Int. J. Struct. Stabil. Dyn.*, **22**(05), p. 2250050. https://doi.org/10.1142/S0219455422500501

Bodaghi, M. and Shakeri, M. (2012), "An analytical approach for free vibration and transient response of functionally graded piezoelectric cylindrical panels subjected to impulsive loads", *Compos. Struct.*, **94**(5), 1721-1735. https://doi.org/10.1016/j.compstruct.2012.01.012

Dastjerdi, S., Akgöz, B. and Civalek, Ö. (2020), "On the effect of viscoelasticity on behavior of gyroscopes", *Int. J. Eng. Sci.*, **149**, p. 103236. https://doi.org/10.1016/j.ijengsci.2019.103236

Foroutan, K., Ahmadi, H. and Carrera, E. (2022), "Free vibration analysis of a sandwich cylindrical shell with an fg core based on the cuf", *Smart Struct. Syst.*, *Int. J.*, **30**(2), 121-133. https://doi.org/10.12989/sss.2022.30.2.121

Guo, H., Du, X. and Żur, K.K. (2021), "On the dynamics of rotating matrix cracked fg-gplrc cylindrical shells via the element-free imls-ritz method", *Eng. Anal. Bound. Elem.*, **131**, 228-239. https://doi.org/10.1016/j.enganabound.2021.06.005

Guo, H., Zhang, C., Fang, H., Rabczuk, T. and Zhuang, X. (2025), "Deep learning to evaluate seismic-induced soil liquefaction and modified transfer learning between various data sources", *Underground Space*. https://doi.org/10.1016/j.undsp.2024.02.001

Komijani, M., Reddy, J. and Eslami, M. (2014), "Nonlinear analysis of microstructure-dependent functionally graded piezoelectric material actuators", *J. Mech. Phys. Solids*, **63**, 214-227. https://doi.org/10.1016/j.jmps.2013.09.004

Liu, B., Wang, Y., Rabczuk, T., Olofsson, T. and Lu, W. (2024), "Multi-scale modeling in thermal conductivity of polyurethane incorporated with phase change materials using physics-informed neural networks", *Renew. Energy*, **220**, p. 119565. https://doi.org/10.1016/j.renene.2023.119565

Long, S.X., Khoo, S.Y., Ong, Z.C., Soong, M.F., Huang, Y.H., Prasath, N. and Noroozi, S. (2024), "A comprehensive review on mechanical amplifier structures in piezoelectric energy harvesters", *Mech. Adv. Mater. Struct.*, **31**(25), 7244-7273. https://doi.org/10.1080/15376494.2023.2282135

Nanthakumar, S., Lahmer, T., Zhuang, X., Zi, G. and Rabczuk, T. (2016), "Detection of material interfaces using a regularized level set method in piezoelectric structures", *Inverse Probl. Sci. Eng.*, **24**(1), 153-176. https://doi.org/10.1080/17415977.2015.1017485

Rabczuk, T., Ren, H. and Zhuang, X. (2019), "A nonlocal operator method for partial differential equations with application to electromagnetic waveguide problem", *Comput. Mater. Continua*, **59**(1), 31-55. https://doi.org/10.32604/cmc.2019.05668

Ramirez, F., Heyliger, P.R. and Pan, E. (2006), "Free vibration response of two-dimensional magneto-electro-elastic laminated plates", *J. Sound Vib.*, **292**(3-5), 626-644. https://doi.org/10.1016/j.jsv.2005.08.006

Reddy, J.N. (2003), *Mechanics of Laminated Composite Plates and Shells*: *Theory and Analysis*, CRC Press. https://doi.org/10.1201/9780203911164

SafarPour, H., Hosseini, M. and Ghadiri, M. (2017), "Influence of three-parameter viscoelastic medium on vibration behavior of a cylindrical nonhomogeneous microshell in thermal environment: an exact solution", *J. Thermal Stress.*, **40**(11), 1353-1367. https://doi.org/10.1080/01495739.2017.1338925

Safarpour, M., Rahimi, A., Alibeigloo, A., Bisheh, H. and Forooghi, A. (2021), "Parametric study of three-dimensional bending and frequency of fg-gplrc porous circular and annular plates on different boundary conditions", *Mech. Based Des. Struct. Mach.*, **49**(5), 707-737. https://doi.org/10.1080/15397734.2020.1719509

Samaniego, E., Anitescu, C., Goswami, S., Nguyen-Thanh, V.M., Guo, H., Hamdia, K., Zhuang, X. and Rabczuk, T. (2020), "An energy approach to the solution of partial differential equations in computational mechanics via machine learning: concepts, implementation and applications", *Comput. Methods Appl. Mech. Eng.*, **362**, p. 112790. https://doi.org/10.1016/j.cma.2019.112790

Sharma, A. (2022), "Effect of porosity on active vibration control of smart structure using porous functionally graded piezoelectric material", *Compos. Struct.*, **280**, p. 114815. https://doi.org/10.1016/j.compstruct.2021.114815

Vel, S.S., Mewer, R. and Batra, R. (2004), "Analytical solution for the cylindrical bending vibration of piezoelectric composite plates", *Int. J. Solids Struct.*, **41**(5-6), 1625-1643. https://doi.org/10.1016/j.ijsolstr.2003.11.010

Wang, Y., Sun, J., Bai, J., Anitescu, C., Eshaghi, M.S., Zhuang, X., Rabczuk, T. and Liu, Y. (2025), "Kolmogorov-arnold-informed neural network: a physics-informed deep learning framework for solving forward and inverse problems based on kolmogorov-arnold networks", *Comput. Methods Appl. Mech. Eng.*, **433**, p. 117518. https://doi.org/10.1016/j.cma.2024.117518

Yang, J. (2010), *Special topics in the theory of piezoelectricity*, Springer Science & Business Media. https://doi.org/10.1007/978-1-4419-1604-9

Zare, R., Najaafi, N., Habibi, M., Ebrahimi, F. and Safarpour, H. (2020), "Influence of imperfection on the smart control frequency characteristics of a cylindrical sensor-actuator gplrc cylindrical shell using a proportional-derivative smart controller", *Smart Struct. Syst.*, *Int. J.*, **26**(4), 469-480. https://doi.org/10.12989/sss.2020.26.4.469

Zerrouki, R., Hamidi, A., Tlidji, Y., Karas, A., Zidour, M. and Tounsi, A. (2022), "Free vibration responses of nonlinear fg-cnt distribution in a polymer matrix", *Smart Struct. Syst.*, *Int. J.*, **30**(2), 135-143. https://doi.org/10.12989/sss.2022.30.2.135